

Observation of contact angle hysteresis due to inhomogeneous electric fields

Wei Wang, Qi Wang, Jia Zhou,* and Antoine Riaud†

State Key Laboratory of ASIC and System, School of Microelectronics, Fudan University, Shanghai 200433, China

(Dated: November 2, 2021)

Static contact angle hysteresis (CAH) is widely attributed to surface roughness and chemical contamination. In the latter case, chemical defects create free-energy barriers that prevent the contact line motion. Electrowetting studies have demonstrated the similar ability of electric fields to alter the surface free-energy landscape. Yet, the increase of apparent static CAH by electric fields remains unseen. Here, we report the observation and theoretical analysis of electrowetting hysteresis. This phenomenon enables the continuous and dynamic control of CAH, not only for fundamental studies but also to manufacture sticky-on-demand surfaces for sample collection.

On most surfaces, the liquid-solid contact angle θ can adopt a range of values before the contact line starts moving [1–3]. This static contact angle hysteresis (CAH, the difference between the advancing and receding contact angles) is mainly attributed to surface roughness [4, 5] and chemical heterogeneities [6, 7]. Despite its major implications [2], CAH remains highly challenging to study experimentally because it is a macroscopic phenomenon excessively sensitive to nanometer-scale defects. Hence, experimental surfaces need to be prepared with the greatest care and quantitative well-controlled experiments are scarce [7, 8]. In most cases, patches of a selected contaminant are carefully deposited on an ultra-clean polished surface. There is a widespread consensus that the contaminant creates free-energy barriers that prevent the contact line motion [1, 9]. This modification of the free-energy landscape is well described by the Gibbs isotherm $\frac{\partial \gamma_0}{\partial \mu_i} = -\Gamma_i$, with Γ_i the surface coverage of a contaminant i , μ_i its chemical potential, and γ_0 the local surface tension. Hence, once the composition of the surface is set, the surface energy landscape is not allowed to vary anymore, which makes CAH experiments extremely work-intensive.

Over the last two decades, electrowetting has emerged as a convenient way to control the apparent contact angle of liquid droplets by adjusting the effective liquid-solid interfacial tension using electric fields [10–19]:

While electrowetting was originally explained by Lippmann on thermodynamic grounds [20], Jones [21] and Buehrle *et al.* [22] have clarified that the liquid-solid interfacial tension and the contact angle are not affected by the electric fields [23], but that the interface profile is gradually evolving from the intrinsic Young-Dupré contact angle to the apparent Young-Lippmann contact angle [24]. This transition length depends on the electrowetting setup but is generally negligible compared to the droplet size as it most often occurs within 1 μm from the contact line.

Outside this transition region, the thermodynamic identity derived by Lippmann is recovered by posing the effective interfacial tension $\gamma = \frac{\partial F}{\partial A}$ as the generalized free energy per unit solid-liquid surface area A [25]. The generalized free-energy $F = E - Q\Phi - \sum_i \mu_i n_i$ offsets the

Helmholtz free-energy E so that it is minimized at thermodynamic equilibrium under fixed electric potential Φ and chemical potential, regardless of the amount n_i of species i and of the electric charge Q . Using Maxwell identities on F yields the celebrated Lippmann equation (additional discussion and derivation available in SI):

$$\frac{\partial \gamma}{\partial \Phi} = -\sigma, \quad (1)$$

with σ the areal surface charge. The striking analogy between Eqn. 1 and the Gibbs isotherm suggests that surface charges and electric fields may also influence the CAH on a scale larger than the electrowetting transition region. Such electrical control of CAH may open exciting strategies for liquid collection and release by reversibly switching the surface between sticky and non-sticky states, respectively. More broadly, it might enable quantitative CAH studies that (i) do not rely on defects and (ii) investigate a continuous range of advancing and receding conditions. To the best of knowledge, this electrically-induced CAH has never been observed. Moreover, most studies in electrowetting phenomena report either no effect [26–28] or even a reduction [29, 30] of CAH due to the application of an electric voltage.

These confusing observations are mainly due to three reasons. First, instead of the static CAH [1–3] observed at mechanical equilibrium, most electrowetting studies are concerned with moving droplets and therefore focus on the more complex dynamic CAH, which involves viscous and inertial forces that may affect the hysteresis [26, 29]. Second, by analogy with chemical heterogeneities and surface roughness, the electrical control of CAH should require inhomogeneous electric fields, which were used only in a handful of reports [27, 31]. We note that homogeneous electric fields can increase the droplet friction by expanding the three-phase contact perimeter [32] or may also alter the CAH by triggering a wetting state transition [33], but the CAH in each state is then controlled by the surface roughness and not by the electric field. Third, the definition of hysteresis differs between electrowetting and the usual wetting phenomena due to chemical heterogeneities and surface roughness. Indeed, the CAH is obtained by recording the onset of

contact line motion, which can be achieved in two ways in electrowetting studies: (i) by hydrostatic stress (such as inclining the plane or pumping the liquid) or (ii) by electrocapillary stress [2, 27, 31]. Since the latter has no direct analog in the chemical and roughness-induced hysteresis, it does not allow to conclude on the ability of electric fields to modify the CAH. Hence, the conditions to observe the variation of CAH due to an electric field have not yet been fulfilled.

Here, we demonstrate the direct analogy of static CAH by applying an inhomogeneous electric field while pumping liquid in the droplet. A thermodynamic model is derived to describe the evolution of advancing and receding apparent contact angles. Similarly to earlier works on CAH [6, 9, 36], our model overlooks the finest details of the contact line structure such as the precursor wetting film [37], Van der Waals force [38] and Lorentz force acting at the interface [22]. Despite these simplifications, it captures well the key features of the experimental observations, including a quadratic dependence on the actuation voltage and an unexpected influence of the droplet contact line radius.

The experimental setup [39], shown in Fig. 1, is similar to the dielectrowetting chip used previously by McHale *et al.* [27]. A periodic array of indium-tin-oxide (ITO) interdigitated electrodes (IDEs, 50 μm finger width and spacing, 130 nm thick) ensures the generation of an inhomogeneous electric field, which is fundamental to observe a CAH. This field is reminiscent of the stripes used in several studies of CAH (see [40] and references therein). A dielectric cyanoethyl pullulan layer (408 nm thick) insulates the liquid from the electrodes [41] so that the whole droplet behaves like an ideal conductor (dielectric relaxation time $\tau_e = \epsilon_l/\sigma_l \simeq 1.3 \times 10^{-4}$ s, with $\epsilon_l \simeq 80\epsilon_0$ and $\epsilon_0 = 8.85 \times 10^{-12}$ F/m the dielectric permittivity of water and vacuum respectively, and $\sigma_l \leq 5.6 \times 10^{-6}$ S/m the conductivity of deionized water). Since electrowetting can only reduce the contact angle, a thin hydrophobic polytetrafluoroethylene (PTFE) layer (60 nm thick) is coated on the dielectric layer to maximize the operating range. A steel tubing is used to replenish or extract liquid during CAH measurements. The tubing is not electrically connected.

For a given voltage, a 40 μL droplet is deposited on the chip and spreads by electrowetting until it reaches a stable shape. Then, the droplet volume is slowly varied by pumping liquid via the tubing. The relatively low flow rate $Q_l = 0.1 \mu\text{L/s}$ ensures (i) that the droplet behaves as an ideal conductor (the characteristic pumping time $\tau_p = V_l/Q_l \simeq 400$ s $\gg \tau_e$ with V_l the droplet volume) and (ii) that the droplet shape is always near mechanical equilibrium ($\tau_{cap} = \sqrt{\frac{\rho_l V_l}{\sigma}} \simeq 23$ ms $\ll \tau_p$ with τ_{cap} the mechanical relaxation time, $\rho_l \simeq 1000$ kg/m³ and $\sigma \simeq 72.8 \times 10^{-3}$ the density and surface tension of water in air) and dynamic CAH can be neglected.

Due to the CAH, the contact line remains trapped during the pumping cycles until the deformation overcomes the static CAH. Hence, advancing and receding contact line radii are the same for a constant voltage. Side view images of the droplet are captured to measure contact angles with a goniometer (DSA30, KRÜSS, Germany). After each acquisition, the surface is cleaned, and the experiment is repeated with a different voltage.

The measured apparent contact angles for U_0 ranging from -100 to +100 V_{DC} are reported in Fig. 2. In agreement with the celebrated Lippmann-Young equation and other electrowetting experiments [11, 13, 42], the contact angle decreases with the voltage until $|U_0|$ reaches approximately 50 V_{DC}, above which electrowetting saturation occurs. Given the controversy surrounding the origins of electrowetting saturation [43–47], we prefer to restrict this study to the low-voltage region ($|U_0| < 90$ V_{DC}).

The static CAH deduced from Fig. 2 is shown in Fig. 3. Unlike other studies [26–30], we observe an increase of CAH (from 3.1° to 7.5°) as $|U_0|$ increases from 0 to 50 V_{DC}. At this point, the CAH features a marked dip before growing far into the saturation regime. The exact reasons for this dip are not yet known but its collocation with the electrowetting saturation suggests that both phenomena might be linked.

In the following, we model the static CAH below saturation regime as a function of the actuation voltage within the framework developed by Johnson and Dettre [6]. The apparent contact angle is obtained by finding the apparent contact line radius R that minimizes the generalized free energy $F = F_{sl} + F_{lg} + F_{sg}$ of the system, with F_{sl} , F_{lg} , and F_{sg} the generalized free energies of the solid-liquid, liquid-gas, and solid-gas interfaces, respectively. The elementary displacement ∂R is taken much smaller than the IDE width [40] but much larger than the transition region (approximately the combined thickness of the hydrophobic and dielectric layers, that is 0.5 μm) so that variations of generalized free energy at the contact line are negligible compared to the variations of solid-liquid free energy. Assuming that hysteresis is weak enough so that the droplet remains circular at all times, which was verified for two orthogonal directions (data available in SI), geometrical construction yields $\partial F_{lg}/\partial R = 2\pi R\gamma_{lg} \cos \theta$ and $\partial F_{sg}/\partial R = -2\pi R\gamma_{sg}$, with γ_{lg} and γ_{sg} the liquid-gas and solid-gas interfacial tensions, respectively [49]. The derivation of $\partial F_{sl}/\partial R$, which differs from the classical Young-Dupré equation [49], is our main concern.

By definition, $F_{sl} = \epsilon_{CL} + \mathcal{C} + \int_0^R \int_{-\pi}^{\pi} \gamma_{sl} r dr d\varphi$ with ϵ_{CL} the free energy in the transition region, \mathcal{C} a constant, γ_{sl} the solid-liquid effective interfacial tension, and φ and r the angular and radial coordinates, respectively (see Fig. 1). Because the transition region is much smaller than the elementary volume that we are studying, ϵ_{CL} is

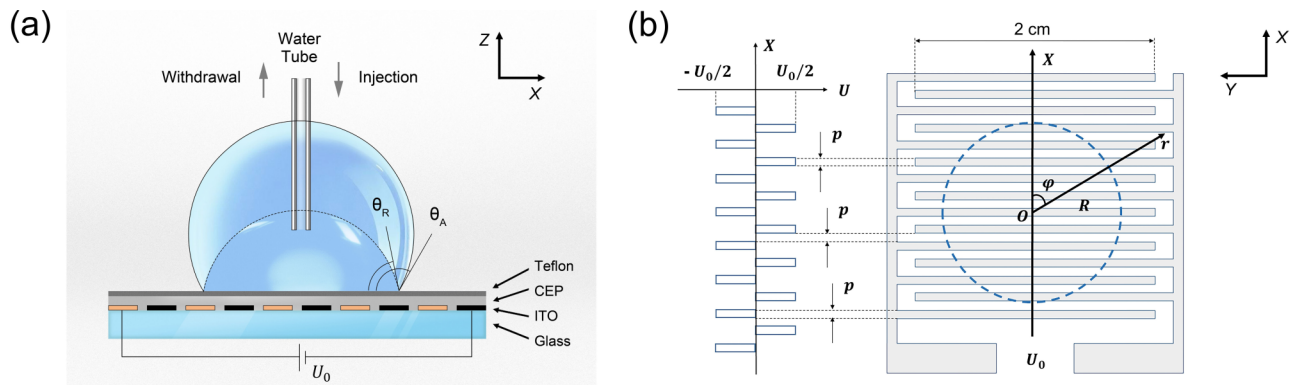


FIG. 1. Experimental setup. (a) Side view. The liquid is replenished or extracted via a steel tubing. The indium tin oxide (ITO) interdigitated electrodes (IDE) are isolated from the liquid by a dielectric layer of cyanoethyl pullulan (CEP) and a hydrophobic layer of Teflon, and connected to a DC supply U_0 . Side-view images were captured and analyzed using a goniometer. (b) Left: Voltage across the solid-liquid interface in x direction. Due to the large aspect ratio of the IDEs, the electric potential is well approximated by a square-wave function [34, 35] with p the finger width and spacing. Right: Top view. The contact line radius of the droplet is denoted by R . In these polar coordinates, the origin O is located at the center of the circular contact area (dashed circle), with φ and r the angular and radial coordinates, respectively.

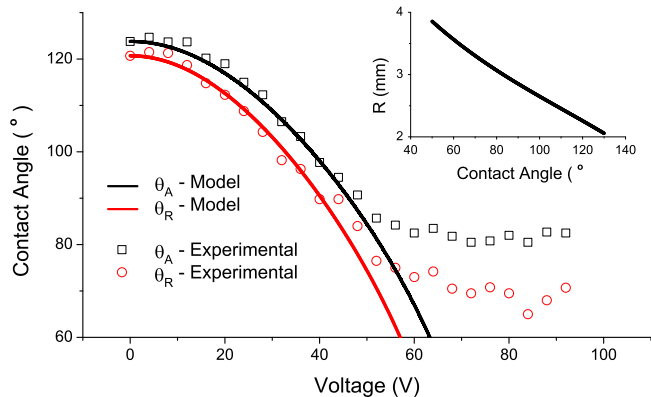


FIG. 2. Effect of the electric voltage on apparent contact angles. The experimental observations agree well with the model (Eqn. 9c and Eqn. 9b) in the low-saturation region ($|U_0| < 50$ V_{DC}). Each experimental dot was averaged over 5 tests and error bars are not presented for the readability. Inset: Contact line radius R versus contact angle for $40 \mu\text{L}$ droplets used in our experiments. It is determined by numerically solving the differential Young-Laplace equation [48].

much smaller than F_{sl} . Elementary calculus yields:

$$\frac{\partial F_{sl}}{\partial R} = R \int_{-\pi}^{\pi} \gamma_{sl} d\varphi. \quad (2)$$

We evaluate γ_{sl} by assuming that the electric field varies continuously at the microscale, and can thus be locally integrated from Eqn. 1:

$$\gamma_{sl} = [\gamma_{sl_0}] - \frac{C}{2} U^2, \quad (3)$$

with U and C the effective voltage across the solid-liquid interface and the areal capacitance between the

electrodes and the liquid (this parameter is determined experimentally in SI). $[\gamma_{sl_0}]$ is the intrinsic interfacial tension, that is γ_{sl} in the absence of electric field. The $[\]$ notation indicates that, due to chemical impurities [1], $[\gamma_{sl_0}]$ is susceptible to vary between a lower and upper bound given by $[\gamma_{sl_0}]$ and $[\gamma_{sl_0}]$ respectively. According to Young-Dupré equation [2], the advancing contact angle θ_{A0} and receding contact angle θ_{R0} at zero-voltage satisfy $\cos \theta_{A0} = (\gamma_{sg} - [\gamma_{sl_0}]) / \gamma_{lg}$ and $\cos \theta_{R0} = (\gamma_{sg} - [\gamma_{sl_0}]) / \gamma_{lg}$, respectively.

For a regular array of IDEs as shown in Fig. 1(b), the effective voltage U is half of the externally applied voltage U_0 (see SI for the full derivation):

$$U^2 = \left(\frac{U_0}{2}\right)^2 \Pi(kx), \quad (4)$$

where Π is the square-wave function denoting the distribution of the electric potential energy (1 above the electrodes and 0 elsewhere, similar to the hysteresis-prone mesa-type landscape of Joanny and De Gennes [36]) and k denotes the wavenumber π/p with p the finger width and also the spacing (see Fig. 1) [34, 35]. Integration of Eqn. 2 is simpler when Π is expressed as a Fourier series:

$$\Pi = \frac{1}{2} + \sum_{n=0}^{\infty} \frac{2(-1)^n}{(2n+1)\pi} \cos[(2n+1)kr \cos \varphi]. \quad (5)$$

Substituting Eqn. 3, 4, and 5 in Eqn. 2 and using the identity $\int_{-\pi}^{\pi} \cos(\tau \cos \varphi) d\varphi = 2\pi J_0(\tau)$ with J_0 the

0-order Bessel function, we get:

$$\frac{\partial F_{sl}}{\partial R} = 2\pi R \{[\gamma_{sl_0}] - \gamma_L - \gamma_H\}, \quad (6a)$$

$$\gamma_L = \frac{CU_0^2}{16}, \quad (6b)$$

$$\gamma_H = \frac{CU_0^2}{8} \sum_{n=0}^{\infty} \frac{2(-1)^n}{(2n+1)\pi} J_0[(2n+1)kR]. \quad (6c)$$

It contains three terms: the intrinsic interfacial tension $[\gamma_{sl_0}]$, the average decrease in effective interfacial tension γ_L (see [31] for IDEs), and an oscillating term γ_H that results in an effective hysteresis effect but did not appear in previous studies. For uniform potential distributions ($k \rightarrow 0$), Eqn. 6a reduces to the standard Lippmann-Young equation. In the current experiments, $R \gg p$, so $J_0(\tau) \simeq \sqrt{\frac{2}{\pi\tau}} \cos(\tau - \frac{\pi}{4})$, which simplifies Eqn. 6c to

$$\gamma_H \approx \frac{CU_0^2}{8\sqrt{\pi k R}} \sum_{n=0}^{\infty} \frac{2\sqrt{2}(-1)^n}{\pi(2n+1)^{3/2}} \cos\left[(2n+1)kR - \frac{\pi}{4}\right]. \quad (7)$$

In the SI, we postulate that the upper and lower bounds of γ_H read:

$$-B \frac{CU_0^2}{16} \sqrt{\frac{p}{R}} < \gamma_H < B \frac{CU_0^2}{16} \sqrt{\frac{p}{R}}, \quad (8)$$

with $B = \frac{4-\sqrt{2}}{\pi^2} \zeta\left(\frac{3}{2}\right) \approx 0.684$ and ζ the Riemann zeta function. Interestingly, Eqn. 8 indicates the dependence of static CAH on $\sqrt{\frac{p}{R}}$.

Finally, substituting Eqn. 8 in Eqn. 6a and minimizing the generalized free energy F yields:

$$\cos \theta_A < \cos \theta < \cos \theta_R \quad (9a)$$

$$\cos \theta_A = \cos \theta_{A0} + \frac{CU_0^2}{16\gamma_{lg}} - B \frac{CU_0^2}{16\gamma_{lg}} \sqrt{\frac{p}{R}} \quad (9b)$$

$$\cos \theta_R = \cos \theta_{R0} + \frac{CU_0^2}{16\gamma_{lg}} + B \frac{CU_0^2}{16\gamma_{lg}} \sqrt{\frac{p}{R}} \quad (9c)$$

The upper and lower bounds of the contact angle in Eqn. 9a correspond to the receding apparent contact angle θ_R and the advancing apparent contact angle θ_A , respectively.

Subtracting Eqn. 9b and Eqn. 9c, and assuming that the CAH remains small yield:

$$\delta \cos \theta_R - \delta \cos \theta_A = B \frac{CU_0^2}{8\gamma_{lg}} \sqrt{\frac{p}{R}} \quad (10a)$$

$$\theta_A - \theta_R = \frac{[\gamma_{sl_0}] - [\gamma_{sl_0}]}{\gamma_{lg} \sin \theta_E} + \frac{BCU_0^2}{8\gamma_{lg} \sin \theta_E} \sqrt{\frac{p}{R}} \quad (10b)$$

with $\delta \cos \theta_i = \cos \theta_i - \cos \theta_i(U=0)$ for $i = R$ or A , and $\theta_E = (\theta_A + \theta_R)/2$. Eqn. 10a provides an energetic viewpoint that singles out the electrical effect on the effective contact angle hysteresis, while Eqn. 10b is a convenient

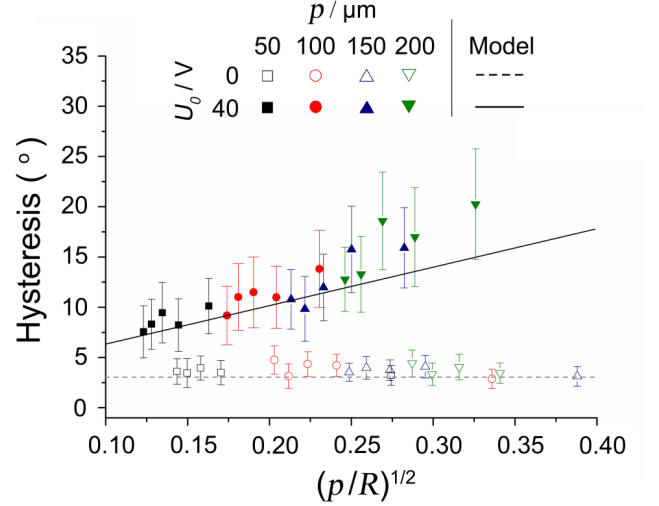


FIG. 3. Contact angle hysteresis measured at 0 and 40 V with electrode pitches ranging from 50 to 200 μm and droplet volumes ranging from 10 to 50 μL . Droplets of larger volumes show smaller hysteresis. The value of R was estimated by solving the Laplace-Young equation. Each experimental dot was averaged over 5 tests. The model was obtained by taking $C = 0.350 \text{ mF/m}^2$, $\gamma_{lg} = 71.97 \text{ mN/m}$, $\theta_{A0} = 123.8^\circ$, and $\theta_{R0} = 120.7^\circ$.

expression for experimental purposes. The first term in Eqn. 10b describes the hysteresis due to surface defects, while the second represents the electrowetting hysteresis. We note that $1/\sin(\theta_E)$ is a decreasing function of the actuation voltage on the studied interval (0 to 40 V) and therefore cannot be responsible for the observed increase in CAH (the contribution of both terms is shown in SI).

The predictions of Eqn. 9 are compared to experimental results in Fig. 2. The areal capacitance $C \simeq 0.350 \text{ mF/m}^2$ (see SI) and the advancing and receding contact angles in the absence of electric field $\theta_{A0} \simeq 123.8^\circ$ and $\theta_{R0} \simeq 120.7^\circ$ are determined by fitting the experimental data. The droplet contact line radius, required in Eqn. 9, is estimated by solving numerically the Young-Laplace equation (see SI). Similarly to previous electrowetting on dielectric (EWOD) studies [11, 13, 42], theory and experiments agree well within the non-saturated region.

Next Eqn. 10b is compared to experimental data in Fig. 3. For the sake of clarity, the comparison is limited to 0 and 40 V for droplet volumes ranging from 10 to 50 μL and electrode pitches from 50 to 200 μm (comparison over a broader range of voltages is available in SI). These experiments were carried out immediately after manufacturing the substrates, resulting in a very low CAH (3.1 $^\circ$) in the absence of electric voltage. Regardless of the electrode pitch, the apparent CAH under 40 V is 3 to 6 times larger than the intrinsic CAH. In good agreement with Eqn. 10b, the apparent CAH scales as $\sqrt{p/R}$ for all the droplet volumes and electrode pitches. Although this

scaling may seem at odds with well-established theories of CAH based on the Cassie-Baxter framework [40], it is a direct consequence of the assumption of weak contact angle hysteresis yielding a circular droplet. As the CAH becomes larger, the droplet contact line should become trapped over the electrodes [27, 40] and follow the better studied regime of contact line motion over strong defects. Using fractal electrodes or electrodes with a broad range of feature sizes would likely yield a more size-independent contact-angle hysteresis. The solid line in Fig. 3 shows the model prediction at 40 V, and confirms the prefactor $\frac{BCU_0^2}{8\gamma_{lg} \sin \theta_E}$. The model begins to underestimate the experimental data at large electrode pitch ($\sqrt{p/R} \simeq 0.25$), after which the droplet starts to lose its circular shape [27, 50] (experimental data for the comparison between contact radii observed in two directions are shown SI).

In summary, we report the experimental control of static apparent CAH by an inhomogeneous electric field, in formal analogy with chemical defects. We derive a thermodynamic model to interpret these observations for small CAH. This regime allows considering a droplet circular at all times, and predicts that the CAH depends on the electrode (defect) pitch, which differs from usual CAH studies involving stronger defects. It is also inferred that the CAH grows quadratically with the actuation voltage. These predictions are confirmed against experimental data, even though the model slightly underestimates the experimental hysteresis at large electrode pitch. This study enables the continuous variation of CAH for fundamental studies, and also provides a feasible approach for on-demand and flexible programming of the CAH.

We are indebted to Kaidi Zhang for the fabrication of the first batch of EWOD devices. This work was supported by the National Natural Science Foundation of China with Grant No. 51950410582, 61874033 and 61674043, the Science Foundation of Shanghai Municipal Government with Grant No. 18ZR1402600, and the State Key Lab of ASIC and System, Fudan University with Grant No. 2018MS003.

* jia.zhou@fudan.edu.cn

† antoine.riaud@fudan.edu.cn

- [1] P. G. De Gennes, Wettings - statics and dynamics, *Rev. Mod. Phys.* **57**, 827 (1985).
- [2] H. B. Eral, D. J. C. M. t. Mannelje, and J. M. Oh, Contact angle hysteresis: a review of fundamentals and applications, *Colloid Polym. Sci.* **291**, 247 (2013).
- [3] H. Y. Erbil, The debate on the dependence of apparent contact angles on drop contact area or three-phase contact line: A review, *Surf. Sci. Rep.* **69**, 325 (2014).
- [4] R. E. J. Johnson and R. H. Dettre, Contact angle hysteresis i. study of an idealized rough surface, in *Contact Angle, Wettability, and Adhesion*, Advances in Chemistry (American Chemical Society, 1964) Chap. 7, pp. 112–135.
- [5] R. G. Cox, The spreading of a liquid on a rough solid surface, *J. Fluid Mech.* **131**, 1 (1983).
- [6] R. E. J. Johnson and R. H. Dettre, Contact angle hysteresis. iii. study of an idealized heterogeneous surface, *J. Phys. Chem.* **68**, 1744 (1964).
- [7] C. Priest, R. Sedev, and J. Ralston, Asymmetric wetting hysteresis on chemical defects, *Phys. Rev. Lett.* **99**, 026103 (2007).
- [8] V. De Johghe and D. Chatain, Experimental study of wetting hysteresis on surfaces with controlled geometrical and/or chemical defects, *Acta metall. mater.* **43**, 1505 (1995).
- [9] R. J. Good, A thermodynamic derivation of wenzel's modification of young's equation for contact angles - together with a theory of hysteresis, *J. Am. Chem. Soc.* **74**, 5041 (1952).
- [10] Q. Sun, D. Wang, Y. Li, J. Zhang, S. Ye, J. Cui, L. Chen, Z. Wang, H.-J. Butt, D. Vollmer, and X. Deng, Surface charge printing for programmed droplet transport, *Nat. Mater.* **18**, 936 (2019).
- [11] F. Mugele and J. C. Baret, Electrowetting: from basics to applications, *J. Phys. Condens. Matter* **17**, R705 (2005).
- [12] R. B. Fair, Digital microfluidics: is a true lab-on-a-chip possible?, *Microfluid. Nanofluid.* **3**, 245 (2007).
- [13] W. Nelson and C. J. Kim, Droplet actuation by electrowetting-on-dielectric (ewod): A review, *J. Adhes. Sci. Technol.* **26**, 1747 (2012).
- [14] J. Heikenfeld, K. Zhou, E. Kreit, B. Raj, S. Yang, B. Sun, A. Milarcik, L. Clapp, and R. Schwartz, Electrofluidic displays using young-laplace transposition of brilliant pigment dispersions, *Nat. Photonics* **3**, 292 (2009).
- [15] R. A. Hayes and B. J. Feenstra, Video-speed electronic paper based on electrowetting, *Nature* **425**, 383 (2003).
- [16] C. Li and H. Jiang, Electrowetting-driven variable-focus microlens on flexible surfaces, *Appl. Phys. Lett.* **100**, 231105 (2012).
- [17] C. Hao, Y. Liu, X. Chen, Y. He, Q. Li, K. Y. Li, and Z. Wang, Electrowetting on liquid-infused film (ewolf): complete reversibility and controlled droplet oscillation suppression for fast optical imaging, *Sci. Rep.* **4**, 6846 (2014).
- [18] J. Heikenfeld, High-transmission electrowetting light valves, *Appl. Phys. Lett.* **86**, 151121 (2005).
- [19] C. U. Murade, J. M. Oh, D. van den Ende, and F. Muggle, Electrowetting driven optical switch and tunable aperture, *Opt. Express* **19**, 15525 (2011).
- [20] M. G. Lippmann, Relation entre les phenomenes electriques et capillaires, *Ann. Chim. Phys.* **5**, 494 (1875).
- [21] T. B. Jones, On the relationship of dielectrophoresis and electrowetting, *Langmuir* **18**, 4437 (2002).
- [22] J. Buehrle, S. Herminghaus, and F. Mugele, Interface profiles near three-phase contact lines in electric fields, *Phys. Rev. Lett.* **91**, 086101 (2003).
- [23] D. Bonn, J. Eggers, J. Indekeu, J. Meunier, and E. Rolley, Wetting and spreading, *Rev. Mod. Phys.* **81**, 739 (2009).
- [24] F. Mugele and J. Buehrle, Equilibrium drop surface profiles in electric fields, *J. Phys.: Condens. Matter* **19**, 375112 (2007).
- [25] J. N. Israelachvili, ed., in *Intermolecular and Surface Forces (Third Edition)* (Academic Press, San Diego, 2011) Chap. 17.1, p. 415, third edition ed.
- [26] W. C. Nelson, P. Sen, and C. J. Kim, Dynamic contact

- angles and hysteresis under electrowetting-on-dielectric, *Langmuir* **27**, 10319 (2011).
- [27] G. McHale, C. V. Brown, M. I. Newton, G. G. Wells, and N. Sampara, Dielectrowetting driven spreading of droplets, *Phys. Rev. Lett.* **107**, 186101 (2011).
- [28] B. Bhushan and Y. Pan, Role of electric field on surface wetting of polystyrene surface, *Langmuir* **27**, 9425 (2011).
- [29] F. Li and F. Mugele, How to make sticky surfaces slippery: Contact angle hysteresis in electrowetting with alternating voltage, *Appl. Phys. Lett.* **92**, 244108 (2008).
- [30] S. Nita, M. Do-Quang, J. Wang, Y. Chen, Y. Suzuki, G. Amberg, and J. Shiomi, Electrostatic cloaking of surface structure for dynamic wetting, *Sci. Adv.* **3**, e1602202 (2017).
- [31] U. C. Yi and C. J. Kim, Characterization of electrowetting actuation on addressable single-side coplanar electrodes, *J. Micromech. Microeng.* **16**, 2053 (2006).
- [32] Y. Wang and B. Bhushan, Liquid microdroplet sliding on hydrophobic surfaces in the presence of an electric field, *Langmuir* **26**, 4013 (2009).
- [33] G. Manukyan, J. M. Oh, D. van den Ende, R. G. H. Lammertink, and F. Mugele, Electrical switching of wetting states on superhydrophobic surfaces: A route towards reversible cassie-to-wenzel transitions, *Phys. Rev. Lett.* **106**, 014501 (2011).
- [34] H. Morgan, A. G. Izquierdo, D. Bakewell, N. G. Green, and A. Ramos, The dielectrophoretic and travelling wave forces generated by interdigitated electrode arrays: analytical solution using fourier series, *J. Phys. D: Appl. Phys.* **34**, 1553 (2001).
- [35] N. S. K. Gunda and S. K. Mitra, Modeling of dielectrophoretic transport of myoglobin molecules in microchannels, *Biomicrofluidics* **4**, 014105 (2010).
- [36] J. F. Joanny and P. G. De Gennes, A model for contact angle hysteresis, *J. Chem. Phys.* **81**, 552 (1984).
- [37] Q. Yuan and Y. P. Zhao, Precursor film in dynamic wetting, electrowetting, and electro-elasto-capillarity, *Phys. Rev. Lett.* **104**, 246101 (2010).
- [38] C. Huh and S. G. Mason, Effects of surface roughness on wetting (theoretical), *J. colloid Interf. Sci.* **60**, 11 (1977).
- [39] W. Wang, Q. Wang, K. Zhang, X. Wang, A. Riaud, and J. Zhou, On-demand contact line pinning during droplet evaporation, *Sens. Actuators, B* , 127983 (2020).
- [40] W. Choi, A. Tuteja, J. M. Mabry, R. E. Cohen, and G. H. McKinley, A modified cassie–baxter relationship to explain contact angle hysteresis and anisotropy on non-wetting textured surfaces, *J. Colloid Interface Sci.* **339**, 208 (2009).
- [41] J. Chen, Y. Yu, K. Zhang, C. Wu, A. Q. Liu, and J. Zhou, Study of cyanoethyl pullulan as insulator for electrowetting, *Sens. Actuators, B* **199**, 183 (2014).
- [42] F. Mugele and S. Herminghaus, Electrostatic stabilization of fluid microstructures, *Appl. Phys. Lett.* **81**, 2302 (2002).
- [43] J. Liu, M. Wang, S. Chen, and M. O. Robbins, Uncovering molecular mechanisms of electrowetting and saturation with simulations, *Phys. Rev. Lett.* **108**, 216101 (2012).
- [44] D. Klarman, D. Andelman, and M. Urbakh, A model of electrowetting, reversed electrowetting, and contact angle saturation, *Langmuir* **27**, 6031 (2011).
- [45] S. Chevalliot, S. Kuiper, and J. Heikenfeld, Experimental validation of the invariance of electrowetting contact angle saturation, *J. Adhe. Sci. Technol.* **26**, 1909 (2012).
- [46] A. G. Papathanasiou, A. T. Papaioannou, and A. G. Boudouvis, Illuminating the connection between contact angle saturation and dielectric breakdown in electrowetting through leakage current measurements, *J. Appl. Phys.* **103**, 034901 (2008).
- [47] V. Peykov, A. Quinn, and J. Ralston, Electrowetting: a model for contact-angle saturation, *Colloid Polym. Sci.* **278**, 789 (2000).
- [48] V. A. Lubarda and K. A. Talke, Analysis of the equilibrium droplet shape based on an ellipsoidal droplet model, *Langmuir* **27**, 10705 (2011).
- [49] P. Roura and J. Fort, Local thermodynamic derivation of young’s equation, *J. Colloid Interface Sci.* **272**, 420 (2004).
- [50] Q. Vo, Y. Fujita, Y. Tagawa, and T. Tran, Anisotropic behaviours of droplets impacting on dielectrowetting substrates, *Soft Matter* , 2621 (2020).